

Refined Rotational Period, Pole Solution & Shape Model for (3200) Phaethon

Megan Ansdell^{1,2}, Karen J. Meech^{1,2}, Olivier Hainaut³, Marc W. Buie⁴, Heather Kaluna^{1,2},
James Bauer⁵, Luke Dundon⁶

mansdell@ifaf.hawaii.edu

ABSTRACT

(3200) Phaethon exhibits both comet- and asteroid-like properties, suggesting it could be a rare transitional object such as a dormant comet or previously volatile-rich asteroid. This justifies detailed study of (3200) Phaethon's physical properties, as a better understanding of asteroid-comet transition objects can provide insight into minor body evolution. We therefore acquired time-series photometry of (3200) Phaethon over 15 nights from 1994 to 2013, primarily using the Tektronix 2048×2048 pixel CCD on the University of Hawaii 2.2-m telescope. We utilized light curve inversion to: (1) refine (3200) Phaethon's rotational period to $P = 3.6032 \pm 0.0008$ h; (2) estimate a rotational pole orientation of $\lambda = +85^\circ \pm 13^\circ$ and $\beta = -20^\circ \pm 10^\circ$; and (3) derive a shape model. We also used our extensive light curve dataset to estimate the slope parameter of (3200) Phaethon's phase curve as $G \sim 0.06$, consistent with C-type asteroids. We discuss how this highly oblique pole orientation with a negative ecliptic latitude supports previous evidence for (3200) Phaethon's origin in the inner main asteroid belt as well as the potential for deeply buried volatiles fueling impulsive yet rare cometary outbursts.

Subject headings: minor planets: individual ((3200) Phaethon), techniques: photometric

¹NASA Astrobiology Institute

²Institute for Astronomy, University of Hawaii, 2680 Woodlawn Drive, Honolulu, HI 96822, USA

³European Southern Observatory, Karl Schwarzschildstrasse 2, 85748 Garching bei Muenchen, Germany

⁴Southwest Research Institute, 1050 Walnut Street, Suite 300, Boulder, CO 80302, USA

⁵Jet Propulsion Laboratory, 4800 Oask Grove Drive, MS 183-401, Pasadena, CA 91109

⁶United States Navy, Washington, DC 20350, USA

1. INTRODUCTION

(3200) Phaethon is a unique minor body in the Solar System, exhibiting both asteroid- and comet-like properties. For example, its unambiguous association with the Geminid meteor stream (Whipple 1983; Gustafson 1989; Williams & Wu 1993) strongly supports a cometary origin, as meteor streams are typically formed from debris left along comet orbits as a result of volatile-driven activity. However, comet-like activity has never been observed in (3200) Phaethon (Hsieh & Jewitt 2005; Wiegert et al. 2008), suggesting a more asteroid-like character (the recurrent dust tail at perihelion recently reported by Jewitt et al. 2013 is unlikely to result from volatile-driven activity). (3200) Phaethon also has features neither distinctly asteroidal nor cometary: its blue color fails to match the typical neutral/red colors of comet nuclei (Lamy et al. 2004) while its spectral shape fails to closely match any meteoritic samples (Licandro et al. 2007). (3200) Phaethon’s orbit also brings it extremely close to the Sun, giving it an unusually small perihelion distance (~ 0.14 AU).

These atypical characteristics justify detailed study of (3200) Phaethon as it could be some form of rare transition object (e.g., an extinct/dormant comet or previously volatile-rich asteroid) that can provide insights into how minor bodies evolve. The combination of its size (~ 5.10 km), albedo (~ 0.11), and near-Earth orbit also allows (3200) Phaethon to periodically appear quite bright from Earth (~ 15 mag), permitting very precise ground-based observations.¹ Thus we have collected an extensive time-series photometry dataset for (3200) Phaethon and employed a light curve inversion technique (Kaasalainen et al. 2001; Kaasalainen & Torppa 2001) to refine the object’s rotational period and pole orientation as well as derive a shape model. We focus on these key physical properties as they have important consequences for an object’s origin and history (e.g., La Spina et al. 2004) as well as its thermophysical properties (e.g., Ohtsuka et al. 2009).

We begin in Section 2 by presenting the observations, data reduction, and time-series photometry that resulted in 16 light curves spanning almost two decades. In Section 3, we use this unprecedentedly large dataset for (3200) Phaethon to refine the object’s rotational period as well as derive a highly oblique rotational pole with a negative ecliptic latitude. In Section 4 we discuss the implications of our findings, namely support for previous evidence of an origin in the inner main asteroid belt as well as the potential for deeply buried volatiles fueling impulsive yet rare cometary outbursts. We conclude in Section 5 with suggestions for future work to further investigate these possible scenarios.

¹Diameter and albedo from IRAS observations (IRAS-A-FPA-3-RDR-IMPS-V6.0)

2. OBSERVATIONS, REDUCTION & PHOTOMETRY

2.1. Observations

We obtained time-series photometry over 15 nights from 1994 to 2013. These observations are summarized in Table 1. All but three nights used the Tektronix 2048×2048 pixel CCD camera on the University of Hawaii 2.2-m telescope on Mauna Kea. Two nights used the PRISM 2048×2048 pixel CCD camera on the Perkins 72-in telescope at the Lowell Observatory in Flagstaff, Arizona, while one night used the Optic 2048×4096 CCD camera also on the University of Hawaii 2.2-m telescope. All observations used the standard Kron-Cousins R filter with the telescope guiding on (3200) Phaethon at non-sidereal rates.

2.2. Reduction & Photometry

Raw images were processed with standard IRAF routines for bias subtraction, flat-fielding, and cosmic ray removal (Tody 1986). We constructed reference flat-fields by median combining dithered images of either twilight or the object field (in both cases, flattening reduced gradients to <1% across the CCD). We performed photometry using the IRAF *phot* routine with circular apertures typically 5'' in radius, although aperture sizes changed depending on the night and/or exposure as they were chosen to consistently include 99.5% of the object's light. Sky subtraction used either an annulus around the photometry aperture or median-combined samples of nearby patches of clear sky. (3200) Phaethon appeared point-like in all images, justifying our use of aperture photometry.

For photometric nights, we calibrated instrumental magnitudes using standard stars from Landolt (1992). The standard stars ranged sufficiently in color and airmass to correct for color terms and extinction, thereby providing absolute flux calibrations. For non-photometric nights, the atmospheric extinction was typically only a few hundredths to tenths of a magnitude. Thus we calibrated these instrumental magnitudes using differential photometry with a large number (20-50) of field stars. Field stars were trailed in all images due to tracking on (3200) Phaethon at non-sidereal rates, so to perform photometry we used aperture sizes that included 99.5% of a typical trailed field star's light for each night. When available, we used Sloan Digital Sky Survey (SDSS; York et al. 2000) magnitudes to recover absolute flux calibrations; we computed transformations between Kron-Cousins and SDSS filters using equations provided on the SDSS website.²

²<http://www.sdss.org>

Unfortunately, SDSS did not cover the star fields of our Nov. 2004 and Dec. 2013 observing runs. For these nights, we used the weighted mean magnitude of each field star across stable periods (or over the entire night, if no period was sufficiently stable) as our reference magnitudes when performing differential photometry. These light curves should therefore be considered relative, rather than absolute. This approach was sufficient for the purposes of our analysis as the light curve inversion technique employed in this work can accommodate relative light curves.

2.3. Lightcurves

Our observations resulted in 16 light curves, as shown in Figure 1. Note that one night (2004/11/21) contained two full light curves, thus 15 nights of observations resulted in 16 full or partial light curves. The supplementary online information contains a table of Julian Date (JD), Universal Time (UT), and R magnitude for each light curve point in our dataset. The light curves span many distinct viewing geometries (i.e., different combinations of ecliptic longitude and latitude) over roughly 20 years. On average, they cover $\sim 75\%$ of a full rotation period with ~ 33 photometry points. Their asymmetric double peaks and significant changes in shape and amplitude over time are probably due to a combination of changing viewing geometries as well as (3200) Phaethon’s high orbital inclination relative to the ecliptic ($\sim 22^\circ$) and its potentially non-spherical shape (see Figure 6).

2.4. Phase Curve

Our dataset spans a wide range of phase angles (α), allowing us to construct a phase curve for (3200) Phaethon. For each night with absolute calibrations, we calculated the reduced R magnitude using the standard equation:

$$H(\alpha) = m(\alpha)_R - 5\log(R\Delta), \quad (1)$$

where $m(\alpha)_R$ is the weighted mean of the observed R magnitudes at a given α , and R and Δ are the associated heliocentric and geocentric distances in AU, respectively. As shown in Figure 2, our dataset only covers the linear portion of (3200) Phaethon’s phase curve. Thus we could strongly constrain G (the slope parameter), but not H (the absolute magnitude), as observations at small phase angles are important for constraining the upturn of the model phase function when using the HG formalism (Bowell et al. 1989). We minimized the residuals between the data and the model phase function, resulting best-fit model parameters of

$H = 13.90$ and $G = 0.06$. This low value of G is consistent with C-type asteroids, which have typical G values of 0.05 ± 0.02 (compared to S-type asteroids with typical G values of 0.23 ± 0.02 ; Lagerkvist & Magnusson 1990). This agrees with (3200) Phaethon’s classification as an F-type (Tholen 1985) or B-type (Green et al. 1985) asteroid, both subtypes of C-type asteroids.

3. PERIOD, POLE ORIENTATION & SHAPE MODEL

3.1. Light Curve Inversion

Light curve inversion is used to derive rotational states and shape models from disk-integrated, time-series photometry. Light curves represent the instantaneous scattered sunlight received at Earth from the projected surface area of a rotating object. The projected surface changes with viewing geometry, affecting the observed light curve amplitude and shape. With data at a sufficient number of different viewing geometries (i.e., different combinations of ecliptic longitude and latitude), it is possible to reconstruct the unprojected shape of the object and solve for its rotational state.

We use the light curve inversion software *convexinv* to refine the rotational period and pole orientation of (3200) Phaethon as well as determine its shape. *Convexinv* uses the light curve inversion scheme described in Kaasalainen et al. (2001) and Kaasalainen & Torppa (2001) to compute a shape-spin-scattering model that gives the best fit to a set of input light curves. The software is available online at the Database of Asteroid Models from Inversion Techniques (DAMIT; Durech et al. 2010).³

3.2. Rotational Period

Previous estimates of (3200) Phaethon’s rotational period used only 2–3 light curves and showed significant spread, from 3.57 ± 0.02 h (Pravec et al. 1998) to 3.604 ± 0.001 h (Meech et al. 1996). We therefore refined (3200) Phaethon’s rotational period by inputting our dataset into the *period_scan* program (part of the *convexinv* package). *Period_scan* searches a user-specified period interval to find the best-fit model to the input light curves, as defined by a minimum relative χ^2 value (χ_{Rel}^2 ; see *convexinv* documentation for details).

We first scanned 1.0–10.0 h to confirm the global χ_{Rel}^2 minimum near ~ 3.6 h, then

³<http://astro.troja.mff.cuni.cz/projects/asteroids3D/web.php>

scanned 3.595–3.610 h at intervals of 3×10^{-5} h to refine this period; Figure 3 shows the resulting χ_{Rel}^2 minimization plot. Because *period_scan* does not take into account observational errors, we determined the best-fit period and associated error using a Monte Carlo approach. We added random Gaussian-distributed noise scaled to typical photometry errors (~ 0.01 mags) to each light curve point, then used *period_scan* to find the period associated with the minimum χ_{Rel}^2 value. We repeated this 100 times, taking the mean and standard deviation of the results as our final period estimate, $P = 3.6032 \pm 0.0008$ h.

3.3. Pole Orientation

To derive pole solutions *convexinv* requires a set of light curves, an estimated rotational period, and an initial guess of pole orientation. Given these inputs the program performs a user-specified number of iterations until converging on a best-fit pole solution defined by a minimum χ_{Rel}^2 value. To find our best-fit pole solution given our uncertainties on (3200) Phaethon’s rotational period, we performed 160 “runs” where each run used a unique period (covering the range found in §3.2 with a resolution of 1×10^{-5} h) and tested a grid of 156 initial pole guesses (equally spaced in ecliptic coordinate space). We took the best-fit solution from each run as that associated with the minimum χ_{Rel}^2 value. The best-fit results from each of these 160 runs are shown in Figure 4 (for ecliptic latitude) and Figure 5 (for ecliptic longitude); there is clear clustering of best-fit results at $\beta \sim -20^\circ$ and $\lambda \sim +85^\circ$. We determined our final pole solution by taking the mean and standard deviation of the results within 10% of the lowest χ_{Rel}^2 value across all runs (in order to filter out poor fits). We also omitted solutions more than $\pm 90^\circ$ from $\lambda \sim +85^\circ$ in order to avoid contamination from possible mirror solutions (due to the 180° degeneracy in λ that is common when using light curve inversion to derive rotational pole orientations). This gave a final pole solution of $\lambda = +85^\circ \pm 13^\circ$ and $\beta = -20^\circ \pm 10^\circ$.

Our results confirm one of the preliminary pole solutions found by Krugly et al. (2002), namely $\lambda_1 = 97^\circ \pm 15^\circ$ and $\beta_1 = -11^\circ \pm 15^\circ$. Thus (3200) Phaethon appears to have a highly oblique rotational pole. Obliquity is the angle between an object’s rotational pole and the normal to its orbital plane, where high obliquity refers to a pole oriented very close to the orbital plane. (3200) Phaethon’s high orbital inclination of $i \approx 22^\circ$ relative to the ecliptic, combined with its longitude of ascending node at $\Omega \approx 256^\circ$, means that the rotational pole derived above could be only $\sim 2^\circ$ above its orbital plane, corresponding to a notably high obliquity of $\sim 88^\circ$.

3.4. Shape Model

Convexinv uses a set of input light curves and a user-defined rotation period and pole orientation to derive a shape model in the form of a convex polyhedron described by a set of triangular facets and vertices (Kaasalainen & Torppa 2001). Prior to this work, a shape model for (3200) Phaethon had not been attempted because of insufficient data and thus uncertain period and pole estimates. Figure 6 presents our shape model for (3200) Phaethon using the rotational period and pole orientation derived above; the axis ratios are $x/y \approx 1.04$ and $x/z \approx 1.14$. We performed a sensitivity analysis by testing period and pole solutions randomly perturbed by our estimated errors. We found that in some cases 3200 Phaethon was predicted to be a long-axis rotator (i.e., $x/z < 1$). This is an interesting result, as long-axis rotation indicates a perturbed state (e.g., Samarasinha et al. 2004). However when visually comparing the model results to the data, our best-fit solutions gave a substantially better fit to the data (see Figure 1) than the perturbed solutions.

4. DISCUSSION

4.1. Preferential Heating at Perihelion

Ohtsuka et al. (2009) performed a detailed thermal analysis of (3200) Phaethon using the preliminary rotational pole initially found by Krugly et al. (2002) and confirmed in this work. They found that (3200) Phaethon’s highly oblique rotational pole, combined with its highly inclined and eccentric orbit, causes preferential heating of its northern hemisphere at perihelion. This is illustrated in Figure 7 (to be compared to Figure 1b in Ohtsuka et al. 2009), which shows (3200) Phaethon’s sub-solar latitude as a function of true anomaly. When (3200) Phaethon is at perihelion (i.e., only 0.14 AU from the Sun) its northern hemisphere appears to be exposed to intense heating.

Ohtsuka et al. (2009) also calculated (3200) Phaethon’s sub-solar equilibrium surface temperature as a function of its orbit (see their Figure 2). They found that at perihelion solar-radiation heating causes the surface temperature of (3200) Phaethon to exceed 800 K, sufficient to decompose and dehydrate minerals such as serpentine phyllosilicates. Ohtsuka et al. (2009) hypothesized that this could result in latitude-dependent color variations on the surface of (3200) Phaethon. Preferential heating would thermally metamorphose and dehydrate phyllosilicates in the more exposed areas, altering the mineralogy to create a visibly bluer surface in the northern hemisphere. They then used previously published spectra to test whether (3200) Phaethon’s spectral gradient became more negative (i.e., bluer) as the sub-Earth point approached the object’s north pole and thus brought more of the

thermally metamorphosed areas into view for an observer on Earth. Although their results hinted at a bluer surface at northern latitudes, they were ultimately inconclusive.

We therefore searched for color variation as a function of sub-Earth latitude using nights from our dataset that contained multi-filter (BVR) photometry supplemented with literature color values (see Table 2). Although none of these observations cover positive sub-Earth latitudes, the northern hemisphere should be increasingly visible for sub-Earth points $> -45^\circ$. We calculated our $B - V$ and $V - R$ colors by interpolating our R magnitudes to the UT times of the other filter measurements, using propagation of errors for subtraction to estimate uncertainties. Due to the fine time sampling of our R -band data (typically ≤ 2 min), uncertainties on the interpolated magnitudes are probably not larger than for the individual measurements. As shown in Table 2, we found that $B - V$ color for (3200) Phaethon does decrease (become bluer) as the sub-Earth point approaches the northern hemisphere. Although $V - R$ color does not show a clear trend, these filters sample redder wavelengths. These results therefore support Ohtsuka et al. (2009)’s prediction of preferential thermal processing in the northern hemisphere of (3200) Phaethon at perihelion.

It is important to note that the color variation predicted by Ohtsuka et al. (2009) requires that the preferential heating of the present planetary epoch be the primary metamorphic heat source of (3200) Phaethon. In other words, (3200) Phaethon could not have been heated to more than a few hundred degrees prior to being injected into its current near-Sun orbit roughly $\sim 10^3$ years ago (corresponding to the age of the Geminids; Gustafson 1989, Ryabova 2007). This is plausible as (3200) Phaethon is classified as an F- or B-type asteroid; these asteroids have been associated with CI/CM carbonaceous chondrites (Hiroi et al. 1996), which are believed to have undergone only moderate heating that can lead to aqueous alteration but not thermal metamorphism.

4.2. Volatile Survival

The evidence for preferential heating of (3200) Phaethon’s northern hemisphere at perihelion, discussed above, raises the possibility of deeply buried volatiles surviving despite an extremely close approach to the Sun. Although a previous calculation of (3200) Phaethon’s core temperature at ~ 250 K (Hsieh & Jewitt 2005) is too high for water ice to survive, this estimate assumed thermal equilibrium. Extreme pole orientations, such as the one found in this work, may allow cooler core temperatures because thermal equilibrium would no longer apply. Boice et al. (2013) performed a more detailed three-dimensional “physico-chemical” modeling of (3200) Phaethon using a highly oblique pole similar to the one found in this work in order to assess whether water ice could still exist in the core of (3200) Phaethon.

They found that (3200) Phaethon is likely to contain relatively pristine volatiles in its interior despite repeated close approaches to the Sun, leaving open the possibility of impulsive outbursts as deeply buried volatiles break through the volatile-depleted surface layers. Thus previous failed attempts to detect comet-like activity on (3200) Phaethon (Hsieh & Jewitt 2005; Wiegert et al. 2008) may have been unsuccessful simply because the observations did not coincide with an outburst.

Although very small amounts of activity at perihelion have been observed in (3200) Phaethon using the space-based STEREO solar observatory, this activity was interpreted to arise from thermal fracture and desiccation cracking due to intense heating at perihelion, rather than comet-like activity from deeply buried volatiles (Jewitt & Li 2010). Moreover, the mass-loss rate from the short-lived dust tails at perihelion are insufficient to account for ongoing replenishment of the Geminid stream, and the dust particles may also be gravitationally unbound to the Solar System, preventing them from contributing to the Geminids (Jewitt et al. 2013).

4.3. Main Belt Origin

(3200) Phaethon has been linked to the main asteroid belt in previous dynamical and compositional studies. Bottke et al. (2002a) used dynamical modeling of (3200) Phaethon’s orbit to show that it has a zero probability of originating from comet reservoirs such as the Jupiter Family Comet region, but a 50% and 80% probability of originating from the central and inner main asteroid belt, respectively. de León et al. (2010) then made the compositional link by showing significant similarities between the reflectance spectra of (3200) Phaethon and another B-type asteroid in the central main belt, 2 Pallas.

The negative ecliptic latitude of (3200) Phaethon’s pole derived in this work supports its origin in the inner main asteroid belt. Objects in near-Earth space have a distinct excess of retrograde spins (Kryszczyńska et al. 2007), which has been postulated to result from the dynamical mechanism that transfers objects from the inner main asteroid belt into near-Earth space—namely the highly efficient ν_6 resonance. Because the ν_6 resonance is located at the inner edge of the main belt, it can only be reached by asteroids with orbits evolving inward toward the Sun. The Yarkovsky effect is the well-known mechanism that alters the orbital semi-major axes of asteroids (see Bottke et al. 2002b for an overview of the influence of the Yarkovsky effect on the dynamical evolution of asteroids), however the Yarkovsky effect only evolves orbits inward for asteroids with retrograde rotations (i.e., $\beta < 0$). Therefore the observed excess of retrograde spins among near-Earth objects has been explained by “dynamical filtering” when retrograde main belt asteroids evolving inward due

to the Yarkovsky effect are preferentially ejected into near-Earth space via the ν_6 resonance (La Spina et al. 2004).

It is important to note that the Yarkovsky effect is less efficient for objects with highly oblique poles, such as (3200) Phaethon. Therefore we must consider alternative mechanisms for altering (3200) Phaethon’s rotational pole to such an extreme orientation while in near-Earth orbit. Collisions can alter rotational pole orientations, although they are highly improbable for an object like (3200) Phaethon due to its small size and the limited population of potential impactors in the inner Solar System. The Yarkovsky-O’Keefe-Radzievskii-Paddack (YORP) effect can also affect spin states, however timescales for changing obliquity by $\sim 90^\circ$ are typically million years (Rubincam 2000); given the young age of the Geminids ($\sim 10^3$ years; Gustafson 1989; Ryabova 2007), it is unlikely that there has been sufficient time for the YORP effect to significantly alter (3200) Phaethon’s rotational state. However, if (3200) Phaethon is indeed still active, variable outbursts may potentially explain the object’s extreme pole orientation.

5. SUMMARY & FUTURE WORK

We have used an extensive time-series photometry dataset, consisting of 16 light curves spanning over 20 years, to refine (3200) Phaethon’s rotational period and pole orientation as well as derive its shape model. We find a period of $P = 3.6032 \pm 0.0008$ h with a pole orientation of $\lambda = +85^\circ \pm 13^\circ$ and $\beta = -20^\circ \pm 10^\circ$. Key areas of future work include confirming surface color variation due to preferential heating at perihelion (e.g., by measuring $B-V$ and $V-R$ colors at positive sub-Earth latitudes) and continuing the search for low-level cometary outbursts (e.g., by serendipitous observation).

Another important area of future work will be deriving pole solutions for the two smaller minor bodies associated with (3200) Phaethon—2005 UD (Jewitt & Hsieh 2006) and 1999 YC (Ohtsuka et al. 2008)—in order to assess their possible formation mechanisms. If all three bodies have randomized pole orientations, this may point to their formation via explosive activity in (3200) Phaethon soon after it was transferred to its current near-Sun orbit from the main belt. Suddenly exposing a volatile-rich (3200) Phaethon to intense heating at perihelion could have resulted in a burst of activity that formed the Geminids, as well as 2005 UD and 1999 YC, leaving (3200) Phaethon dormant/extinct. This is an enticing interpretation given that the Geminids is a dynamically young meteor stream, which suggests ongoing activity, yet (3200) Phaethon has exhibited no known comet-like outbursts sufficient to replenish the stream. Simultaneous formation of the Geminids, 2005 UD, and 1999 YC with extinction/dormancy of (3200) Phaethon would account for both the youth of the

Geminids as well as the lack of activity seen in (3200) Phaethon. However because such an event could significantly alter rotational states, the negative ecliptic latitude of (3200) Phaethon’s pole would no longer be evidence for its origin in the inner main belt (although this would not preclude a possible origin in the main belt).

We thank the referee for their very detailed review of this work, which greatly improved the paper. We are extremely grateful to the telescope staff of UH88 and Lowell Observatory, without whom this work would not have been possible. A special thanks to Michael Belton for his insightful feedback on short notice. We also thank Josef Ďurech and his collaborators, who kindly provided the MATLAB code used to generate the shape model visualization. This work was supported by the National Aeronautics and Space Administration through the NASA Astrobiology Institute under Cooperative Agreement No. NNA04CC08A issued through the Office of Space Science, by NASA Grant Nos. NAGW 5015, NAG5-4495, NNX07A044G, NNX13A151G, and NNX07AF79G. Image processing was done in part using the IRAF software. IRAF is distributed by the National Optical Astronomy Observatories, which is operated by the Association of Universities for Research in Astronomy, Inc. (AURA) under cooperative agreement with the National Science Foundation.

REFERENCES

- Boice, D. C., Benkhoff, J., & Huebner, W. F. 2013, in AAS/Division for Planetary Sciences Meeting Abstracts, Vol. 45, AAS/Division for Planetary Sciences Meeting Abstracts, 413.32
- Bottke, W. F., Morbidelli, A., Jedicke, R., Petit, J.-M., Levison, H. F., Michel, P., & Metcalfe, T. S. 2002a, *Icarus*, 156, 399
- Bottke, Jr., W. F., Vokrouhlický, D., Rubincam, D. P., & Broz, M. 2002b, *Asteroids III*, 395
- Bowell, E., Hapke, B., Domingue, D., Lumme, K., Peltoniemi, J., & Harris, A. W. 1989, in *Asteroids II*, ed. R. P. Binzel, T. Gehrels, & M. S. Matthews, 524–556
- de León, J., Campins, H., Tsiganis, K., Morbidelli, A., & Licandro, J. 2010, *A&A*, 513, A26
- Dundon, L. 2005, Master’s thesis, University of Hawaii
- Ďurech, J., Sidorin, V., & Kaasalainen, M. 2010, *A&A*, 513, A46
- Green, S. F., Meadows, A. J., & Davies, J. K. 1985, *MNRAS*, 214, 29P

- Gustafson, B. A. S. 1989, *A&A*, 225, 533
- Harris, A. W. 1994, *Icarus*, 107, 209
- Hiroi, T., Zolensky, M. E., Pieters, C. M., & Lipschutz, M. E. 1996, *Meteoritics and Planetary Science*, 31, 321
- Hsieh, H. H., & Jewitt, D. 2005, *ApJ*, 624, 1093
- Jewitt, D. 2013, *AJ*, 145, 133
- Jewitt, D., & Hsieh, H. 2006, *AJ*, 132, 1624
- Jewitt, D., & Li, J. 2010, *AJ*, 140, 1519
- Jewitt, D., Li, J., & Agarwal, J. 2013, *ApJ*, 771, L36
- Kaasalainen, M., & Torppa, J. 2001, *Icarus*, 153, 24
- Kaasalainen, M., Torppa, J., & Muinonen, K. 2001, *Icarus*, 153, 37
- Kasuga, T., & Jewitt, D. 2008, *AJ*, 136, 881
- Krugly, Y. N., et al. 2002, *Icarus*, 158, 294
- Kryszczyńska, A., La Spina, A., Paolicchi, P., Harris, A. W., Breiter, S., & Pravec, P. 2007, *Icarus*, 192, 223
- La Spina, A., Paolicchi, P., Kryszczyńska, A., & Pravec, P. 2004, *Nature*, 428, 400
- Lagerkvist, C.-I., & Magnusson, P. 1990, *A&AS*, 86, 119
- Lamy, P. L., Toth, I., Fernandez, Y. R., & Weaver, H. A. 2004, *Comets II* (University of Arizona Press), 223–264
- Landolt, A. U. 1992, *aj*, 104, 340
- Licandro, J., Campins, H., Mothé-Diniz, T., Pinilla-Alonso, N., & de León, J. 2007, *A&A*, 461, 751
- Meech, K. J., R., H. O., W., B. M., A’Hearn, M. F., & Lisse, C. 1996, *Abstracts of ACM*, 42
- Ohtsuka, K., Arakida, H., Ito, T., Yoshikawa, M., & Asher, D. J. 2008, *Meteoritics and Planetary Science Supplement*, 43, 5055

- Ohtsuka, K., Nakato, A., Nakamura, T., Kinoshita, D., Ito, T., Yoshikawa, M., & Hasegawa, S. 2009, PASJ, 61, 1375
- Pravec, P., Wolf, M., & Šarounová, L. 1998, Icarus, 136, 124
- Rubincam, D. P. 2000, Icarus, 148, 2
- Ryabova, G. O. 2007, MNRAS, 375, 1371
- Samarasinha, N. H., Mueller, B. E. A., Belton, M. J. S., & Jorda, L. 2004, Rotation of cometary nuclei, ed. G. W. Kronk (Arizona University Press), 281–299
- Tholen, D. J. 1985, IAU Circ., 4034, 2
- Tody, D. 1986, in Society of Photo-Optical Instrumentation Engineers (SPIE) Conference Series, Vol. 627, Instrumentation in astronomy VI, ed. D. L. Crawford, 733
- Whipple, F. L. 1983, IAU Circ., 3881, 1
- Wiegert, P. A., Houde, M., & Peng, R. 2008, Icarus, 194, 843
- Williams, I. P., & Wu, Z. 1993, MNRAS, 262, 231
- York, D. G., et al. 2000, AJ, 120, 1579

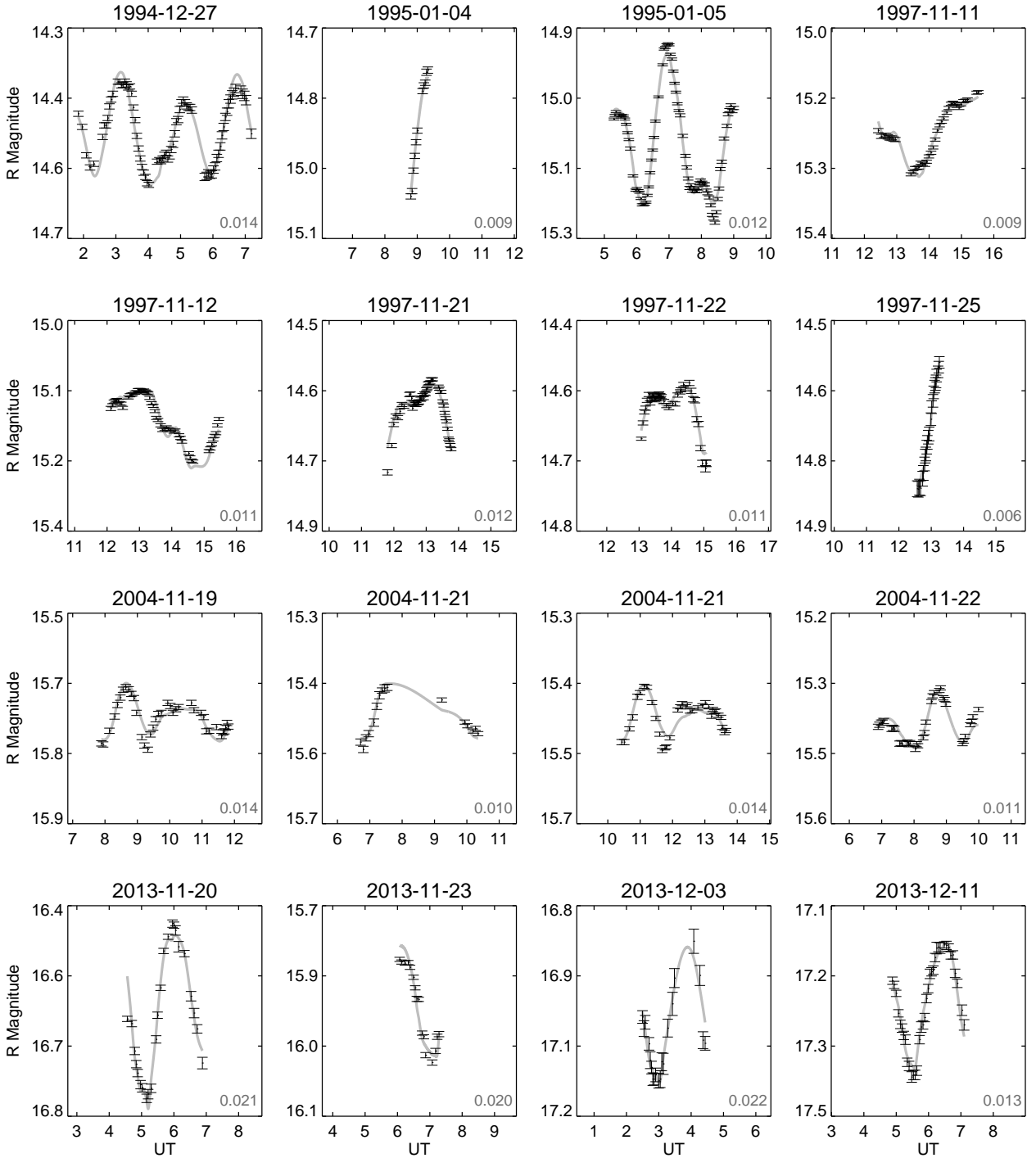


Fig. 1.— Observed and model light curves of (3200) Phaethon. Observed light curves are shown in black with associated errors, while model light curves using our derived period and pole solutions are shown in gray. The RMS values between the observed and model light curves at each epoch are given in the lower right corners.

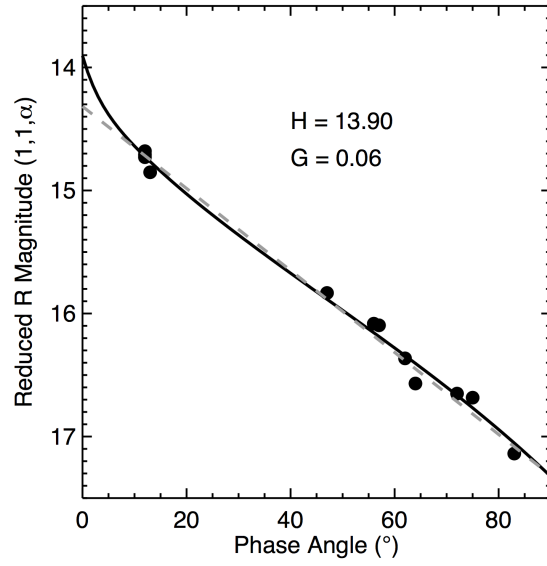


Fig. 2.— Phase curve of (3200) Phaethon. The gray dashed line is the linear least-squares fit to the black data points (errors on the data are smaller than the symbols). The black curve is the best-fit phase curve model using the HG formalism, where $H = 13.90$ and $G = 0.06$.

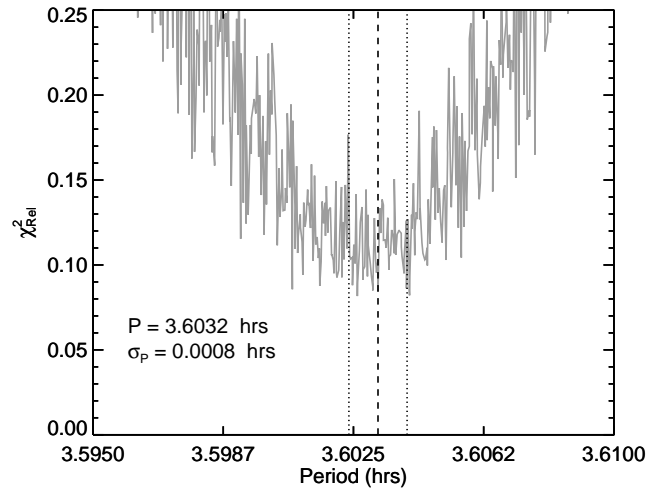


Fig. 3.— χ_{Rel}^2 minimization plot for the rotational period of (3200) Phaethon output from *period_scan*. Dashed line shows our final period estimate of $P = 3.6032$ h, while dotted lines show our estimated errors of $\sigma_P = 0.0008$ h. Because *period_scan* does not consider observational errors, we used a Monte Carlo method to determine these values (see §3.2).

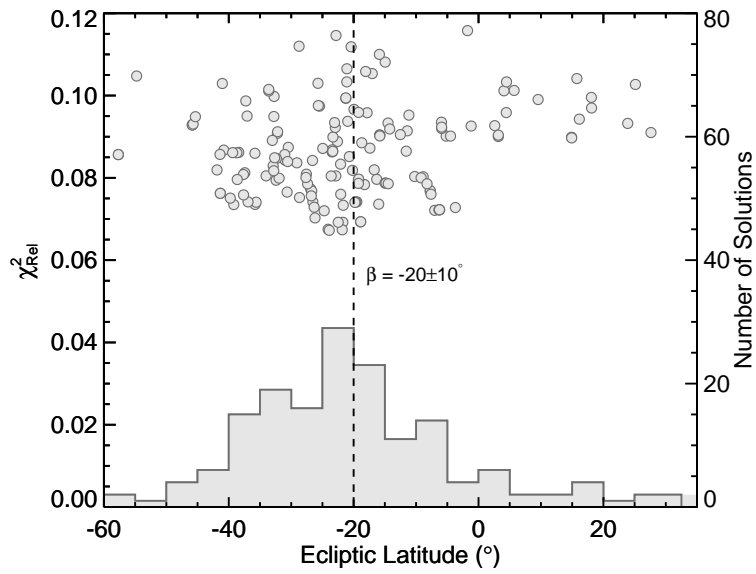


Fig. 4.— Best-fit ecliptic latitude solutions output from *convexinv* across our range of possible periods. The histogram shows clear clustering of best-fit solutions at $\beta \sim -20^\circ$, while the χ^2_{Rel} points show a trend toward minimum values also at $\beta \sim -20^\circ$. The final pole solution, $\beta = -20 \pm 10^\circ$ (dashed line), was found using the mean and standard deviation of all solutions within 10% of the lowest χ^2_{Rel} value.

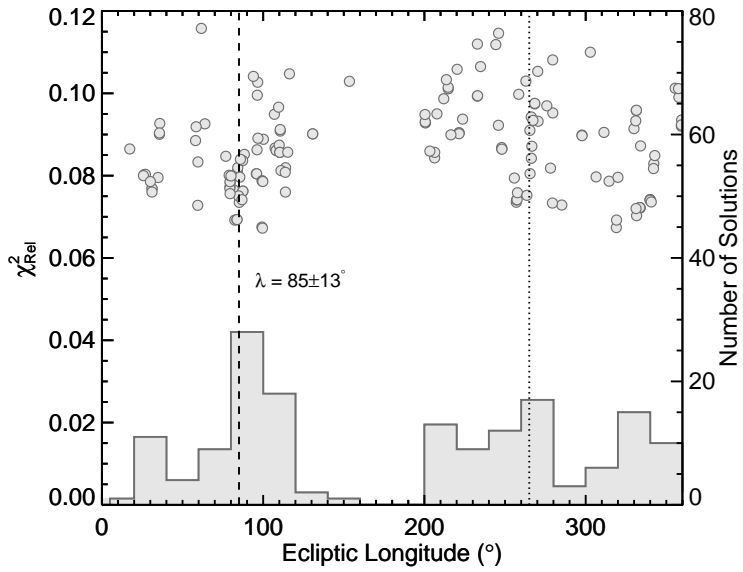


Fig. 5.— Best-fit ecliptic longitude solutions output from *convexinv* across our range of possible periods. The histogram shows clear clustering of best-fit solutions at $\lambda \sim 90^\circ$, while the χ^2_{Rel} points show a trend toward minimum values also at $\lambda \sim 90^\circ$. The final pole solution, $\lambda = 85 \pm 13^\circ$ (dashed line), was found using the mean and standard deviation of all solutions within 10% of the lowest χ^2_{Rel} value (after rejecting all solutions more than $\pm 90^\circ$ from $\lambda \sim 90^\circ$ to avoid contamination from possible mirror solutions). The dotted line shows a possible 180° mirror solution.

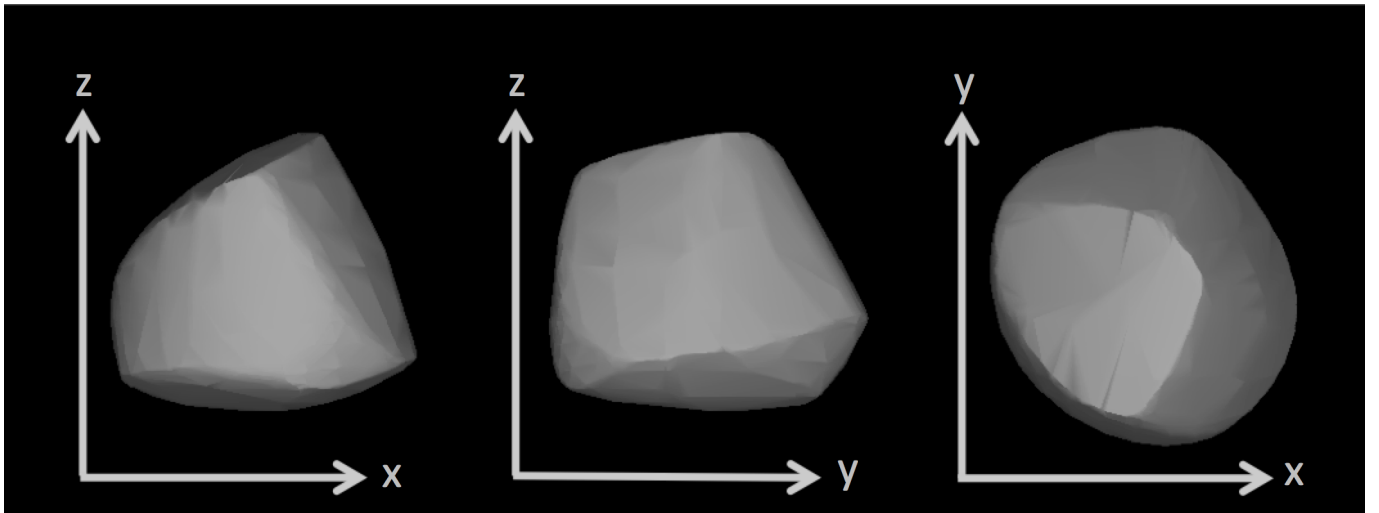


Fig. 6.— Shape model of (3200) Phaethon derived using our best-fit period and pole solutions. The model is shown in three orthogonal views: the left and center panels show equatorial views that are 90° apart (pole oriented upwards) while the right panel shows a pole-on view (pole oriented out of the page). The axis ratios are $x/y \approx 1.04$ and $x/z \approx 1.14$.

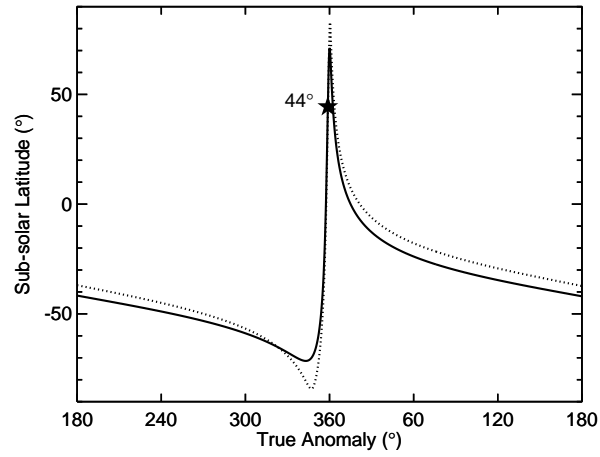


Fig. 7.— Variations in sub-solar latitude along (3200) Phaethon’s orbit. The star indicates perihelion, when the sub-solar point on (3200) Phaethon is at $\sim 44^\circ$ latitude. The solid line shows the sub-solar latitude when using the pole orientation derived in this work. The dotted line shows the sub-solar latitude when using the pole orientation derived by Krugly et al. (2002) and used in the thermal analysis of Ohtsuka et al. (2009). Both indicate that (3200) Phaethon experiences preferential heating of its northern hemisphere at perihelion.

Table 1. (3200) Phaethon Dataset

Obs. Date (UT)	Instrument	Observer(s)	Weather	Seeing (")	# Obs. ^a	Expt. ^b	% Rot. ^c	RN ^d	Gn ^e	Δ	R	λ	β	α
1994/12/27	PRISM	Buie	Photometric	1.6	76	13680	149	7.2	2.7	0.44	1.22	28	10	47
1995/01/04	Tektronix	Meech & Hainaut	Photometric	0.6	11	1100	15	10.0	1.8	0.46	1.11	16	6	62
1995/01/05	Tektronix	Meech & Hainaut	Photometric	0.7	79	7860	103	10.0	1.8	0.46	1.09	15	6	64
1997/11/11	Tektronix	Meech & Bauer	Photometric	1.3	39	5850	86	6.0	1.8	0.57	1.18	133	7	56
1997/11/12	Tektronix	Meech & Bauer	Photometric	1.2	52	6240	93	6.0	1.8	0.55	1.17	135	7	57
1997/11/21	Tektronix	Meech & Bauer	Photometric	1.0	48	2880	55	6.0	1.8	0.38	1.03	153	5	72
1997/11/22	Tektronix	Meech & Bauer	Photometric	0.8	41	1260	81	6.0	1.8	0.38	1.01	156	4	75
1997/11/25	Tektronix	Meech & Bauer	Photometric	0.5	24	720	19	6.0	1.8	0.34	0.96	166	3	83
2004/11/19	Tektronix	Dundon	Cirrus	0.9	38	1860	109	6.0	1.8	0.84	1.78	76	17	13
2004/11/21a	Tektronix	Dundon	Cirrus	1.0	16	640	101	6.0	1.8	0.81	1.76	75	17	12
2004/11/21b	Tektronix	Dundon	Cirrus	1.0	35	1400	90	6.0	1.8	0.81	1.76	75	17	12
2004/11/22	Tektronix	Dundon	Cirrus	1.1	35	1400	86	6.0	1.8	0.80	1.75	74	17	12
2013/11/20	Tektronix	Dundon	Cirrus	0.9	24	2880	65	14.0	1.8	0.79	1.07	308	28	62
2013/11/23	Optic	Ansdell	Cirrus	0.9	16	2400	34	4.0	1.4	0.84	1.12	314	28	58
2013/12/03	PRISM	Meech & Ansdell	Cirrus	2.4	20	3030	54	7.2	2.7	1.02	1.26	328	25	50
2013/12/11	Tektronix	Ansdell	Photometric	1.3	26	3900	62	14.0	1.8	1.17	1.37	336	23	45

^aNumber of data points in light curve. ^bTotal exposure time (s). ^cPercent of rotation period covered. ^dRead noise (e^-). ^eGain (e^-/ADU).

Table 2. (3200) Phaethon Surface Color Variation

UT	True Anomaly ($^{\circ}$)	Sub-Earth Latitude ($^{\circ}$)	$B - V$	$V - R$	Reference
2010/09/10	201	-62	0.67 ± 0.02	0.32 ± 0.02	Jewitt (2013)
2007/09/04	193	-62	0.61 ± 0.01	0.34 ± 0.03	Kasuga & Jewitt (2008)
2004/11/19	197	-50	0.59 ± 0.01	0.35 ± 0.01	Dundon (2005)
1997/11/12	210	-40	0.58 ± 0.01	0.34 ± 0.02	This work
1997/11/22	214	-22	0.57 ± 0.01	0.36 ± 0.01	This work
1995/01/04	211	-11	0.52 ± 0.01	0.33 ± 0.01	This work

Table 3. Observed Light Curves of (3200) Phaethon^a

JD	UT	R	σ_R
2449713.5767	1.8418	14.452	0.005
2449713.5817	1.9598	14.477	0.005
2449713.5870	2.0878	14.531	0.005
2449713.5917	2.2020	14.554	0.005
2449713.5965	2.3170	14.547	0.005
2449713.6079	2.5906	14.496	0.005
2449713.6101	2.6431	14.474	0.005
2449713.6123	2.6959	14.474	0.005
2449713.6145	2.7487	14.460	0.005
2449713.6167	2.8018	14.438	0.005
2449713.6189	2.8541	14.425	0.005
2449713.6211	2.9069	14.414	0.005
2449713.6277	3.0653	14.391	0.005
2449713.6299	3.1183	14.391	0.005
2449713.6321	3.1711	14.398	0.005
2449713.6343	3.2239	14.397	0.005
2449713.6365	3.2765	14.391	0.005
2449713.6387	3.3295	14.396	0.005
2449713.6409	3.3818	14.402	0.005
2449713.6431	3.4346	14.400	0.005
2449713.6453	3.4874	14.414	0.005
2449713.6475	3.5405	14.440	0.005
2449713.6499	3.5969	14.464	0.005
2449713.6521	3.6497	14.494	0.005
2449713.6543	3.7027	14.518	0.005
2449713.6565	3.7555	14.537	0.005
2449713.6587	3.8081	14.553	0.005
2449713.6609	3.8609	14.564	0.005
2449713.6631	3.9137	14.572	0.005
2449713.6653	3.9667	14.584	0.005
2449713.6675	4.0195	14.587	0.005
2449713.6781	4.2737	14.543	0.005
2449713.6810	4.3440	14.540	0.005
2449713.6832	4.3966	14.542	0.005
2449713.6854	4.4494	14.537	0.005
2449713.6876	4.5024	14.530	0.005
2449713.6898	4.5550	14.526	0.005
2449713.6920	4.6078	14.538	0.006
2449713.6942	4.6606	14.532	0.006
2449713.6964	4.7134	14.520	0.006
2449713.6986	4.7662	14.510	0.006
2449713.7008	4.8190	14.490	0.006
2449713.7030	4.8718	14.467	0.006
2449713.7052	4.9246	14.463	0.006
2449713.7074	4.9771	14.444	0.006
2449713.7096	5.0299	14.431	0.006

Table 3—Continued

JD	UT	R	σ_R
2449713.7118	5.0827	14.426	0.006
2449713.7140	5.1358	14.431	0.006
2449713.7162	5.1883	14.437	0.006
2449713.7184	5.2411	14.440	0.006
2449713.7206	5.2939	14.440	0.006
2449713.7228	5.3467	14.445	0.006
2449713.7395	5.7482	14.572	0.007
2449713.7419	5.8054	14.570	0.007
2449713.7441	5.8582	14.565	0.007
2449713.7463	5.9107	14.568	0.007
2449713.7485	5.9635	14.567	0.007
2449713.7507	6.0163	14.558	0.007
2449713.7529	6.0691	14.552	0.007
2449713.7551	6.1219	14.536	0.007
2449713.7573	6.1747	14.528	0.007
2449713.7595	6.2275	14.514	0.007
2449713.7617	6.2806	14.493	0.007
2449713.7639	6.3331	14.477	0.007
2449713.7661	6.3859	14.458	0.007
2449713.7683	6.4387	14.448	0.007
2449713.7705	6.4918	14.433	0.008
2449713.7727	6.5441	14.424	0.008
2449713.7749	6.5969	14.416	0.008
2449713.7771	6.6497	14.411	0.008
2449713.7793	6.7025	14.404	0.008
2449713.7860	6.8647	14.408	0.009
2449713.7882	6.9178	14.414	0.009
2449713.7904	6.9703	14.418	0.009
2449713.7926	7.0231	14.426	0.009
2449713.7994	7.1866	14.490	0.009
2449721.8667	8.8019	15.032	0.005
2449721.8684	8.8414	15.022	0.005
2449721.8702	8.8839	14.983	0.005
2449721.8719	8.9244	14.955	0.005
2449721.8735	8.9642	14.929	0.005
2449721.8752	9.0047	14.907	0.005
2449721.8819	9.1664	14.832	0.005
2449721.8836	9.2067	14.821	0.005
2449721.8853	9.2472	14.816	0.005
2449721.8870	9.2872	14.796	0.006
2449721.8886	9.3275	14.792	0.006
2449722.7206	5.2953	15.030	0.002
2449722.7220	5.3269	15.023	0.002
2449722.7234	5.3611	15.016	0.002
2449722.7274	5.4581	15.022	0.002
2449722.7297	5.5128	15.026	0.002

Table 3—Continued

JD	UT	R	σ_R
2449722.7307	5.5367	15.023	0.002
2449722.7331	5.5933	15.024	0.002
2449722.7348	5.6353	15.030	0.002
2449722.7365	5.6758	15.040	0.002
2449722.7383	5.7194	15.056	0.002
2449722.7400	5.7594	15.069	0.002
2449722.7417	5.8014	15.086	0.003
2449722.7453	5.8869	15.138	0.002
2449722.7487	5.9686	15.165	0.002
2449722.7504	6.0086	15.162	0.002
2449722.7521	6.0494	15.166	0.002
2449722.7537	6.0900	15.169	0.002
2449722.7554	6.1294	15.181	0.002
2449722.7570	6.1686	15.193	0.002
2449722.7587	6.2086	15.193	0.002
2449722.7604	6.2492	15.192	0.002
2449722.7622	6.2931	15.188	0.002
2449722.7639	6.3331	15.175	0.002
2449722.7655	6.3731	15.159	0.002
2449722.7672	6.4131	15.132	0.002
2449722.7690	6.4558	15.108	0.002
2449722.7707	6.4961	15.089	0.002
2449722.7723	6.5361	15.065	0.002
2449722.7741	6.5778	15.034	0.002
2449722.7781	6.6756	14.988	0.002
2449722.7835	6.8047	14.927	0.002
2449722.7852	6.8458	14.897	0.002
2449722.7869	6.8867	14.894	0.002
2449722.7886	6.9272	14.889	0.002
2449722.7903	6.9672	14.887	0.002
2449722.7920	7.0072	14.889	0.002
2449722.7936	7.0469	14.907	0.002
2449722.7953	7.0883	14.916	0.002
2449722.7972	7.1317	14.939	0.002
2449722.7989	7.1725	14.962	0.002
2449722.8006	7.2133	14.979	0.002
2449722.8024	7.2581	15.001	0.002
2449722.8043	7.3036	15.014	0.002
2449722.8060	7.3444	15.023	0.003
2449722.8094	7.4264	15.062	0.003
2449722.8129	7.5100	15.100	0.003
2449722.8146	7.5500	15.122	0.003
2449722.8163	7.5914	15.143	0.003
2449722.8182	7.6364	15.161	0.003
2449722.8200	7.6800	15.156	0.003
2449722.8217	7.7214	15.166	0.003

Table 3—Continued

JD	UT	R	σ_R
2449722.8234	7.7625	15.162	0.003
2449722.8252	7.8047	15.166	0.003
2449722.8270	7.8486	15.167	0.003
2449722.8289	7.8947	15.162	0.003
2449722.8308	7.9394	15.152	0.003
2449722.8325	7.9800	15.147	0.003
2449722.8343	8.0225	15.151	0.003
2449722.8360	8.0639	15.154	0.003
2449722.8378	8.1061	15.154	0.003
2449722.8395	8.1483	15.166	0.003
2449722.8413	8.1906	15.171	0.003
2449722.8433	8.2403	15.179	0.003
2449722.8453	8.2883	15.194	0.003
2449722.8472	8.3317	15.212	0.003
2449722.8489	8.3747	15.219	0.003
2449722.8508	8.4181	15.227	0.003
2449722.8526	8.4614	15.207	0.003
2449722.8544	8.5047	15.182	0.003
2449722.8561	8.5456	15.162	0.003
2449722.8578	8.5869	15.125	0.003
2449722.8595	8.6289	15.111	0.003
2449722.8625	8.6997	15.067	0.003
2449722.8661	8.7856	15.043	0.003
2449722.8678	8.8264	15.021	0.003
2449722.8697	8.8717	15.013	0.003
2449722.8712	8.9094	15.004	0.003
2449722.8732	8.9558	15.015	0.003
2449722.8751	9.0017	15.009	0.003
2450764.0178	12.4283	15.219	0.004
2450764.0218	12.5228	15.230	0.004
2450764.0254	12.6092	15.228	0.004
2450764.0278	12.6667	15.228	0.004
2450764.0302	12.7244	15.231	0.004
2450764.0325	12.7806	15.233	0.004
2450764.0353	12.8475	15.233	0.004
2450764.0375	12.9011	15.235	0.004
2450764.0398	12.9558	15.236	0.004
2450764.0598	13.4364	15.302	0.003
2450764.0628	13.5081	15.298	0.003
2450764.0652	13.5656	15.290	0.003
2450764.0675	13.6208	15.290	0.003
2450764.0699	13.6783	15.289	0.003
2450764.0725	13.7408	15.280	0.003
2450764.0750	13.8003	15.282	0.003
2450764.0780	13.8711	15.284	0.003
2450764.0802	13.9247	15.278	0.003

Table 3—Continued

JD	UT	R	σ_R
2450764.0831	13.9933	15.268	0.003
2450764.0858	14.0594	15.261	0.003
2450764.0885	14.1242	15.251	0.003
2450764.0912	14.1883	15.236	0.003
2450764.0941	14.2594	15.219	0.003
2450764.0969	14.3244	15.209	0.003
2450764.0995	14.3878	15.202	0.003
2450764.1021	14.4497	15.196	0.003
2450764.1061	14.5467	15.185	0.003
2450764.1086	14.6075	15.176	0.003
2450764.1117	14.6803	15.168	0.003
2450764.1140	14.7358	15.166	0.003
2450764.1162	14.7900	15.168	0.003
2450764.1188	14.8512	15.172	0.003
2450764.1219	14.9256	15.176	0.003
2450764.1244	14.9864	15.169	0.003
2450764.1276	15.0622	15.163	0.003
2450764.1302	15.1258	15.162	0.003
2450764.1329	15.1892	15.160	0.003
2450764.1446	15.4700	15.147	0.003
2450764.1467	15.5214	15.146	0.003
2450765.0048	12.1161	15.123	0.004
2450765.0070	12.1672	15.117	0.003
2450765.0088	12.2117	15.110	0.003
2450765.0107	12.2558	15.108	0.003
2450765.0125	12.3006	15.107	0.003
2450765.0144	12.3464	15.109	0.003
2450765.0164	12.3928	15.113	0.003
2450765.0183	12.4392	15.114	0.003
2450765.0202	12.4847	15.122	0.003
2450765.0276	12.6625	15.102	0.003
2450765.0294	12.7067	15.098	0.003
2450765.0313	12.7503	15.097	0.003
2450765.0331	12.7936	15.096	0.003
2450765.0360	12.8647	15.093	0.003
2450765.0381	12.9142	15.092	0.003
2450765.0399	12.9575	15.088	0.003
2450765.0417	13.0019	15.088	0.003
2450765.0436	13.0453	15.088	0.003
2450765.0454	13.0906	15.090	0.003
2450765.0473	13.1353	15.089	0.003
2450765.0492	13.1800	15.091	0.003
2450765.0510	13.2244	15.093	0.003
2450765.0529	13.2689	15.094	0.003
2450765.0548	13.3150	15.103	0.003
2450765.0571	13.3711	15.113	0.003

Table 3—Continued

JD	UT	R	σ_R
2450765.0595	13.4286	15.118	0.003
2450765.0615	13.4750	15.128	0.003
2450765.0634	13.5214	15.141	0.003
2450765.0656	13.5742	15.145	0.003
2450765.0689	13.6539	15.155	0.003
2450765.0714	13.7136	15.164	0.003
2450765.0743	13.7833	15.162	0.003
2450765.0765	13.8356	15.159	0.003
2450765.0787	13.8894	15.162	0.003
2450765.0815	13.9564	15.164	0.003
2450765.0859	14.0628	15.167	0.003
2450765.0878	14.1078	15.165	0.003
2450765.0927	14.2242	15.174	0.003
2450765.0945	14.2692	15.179	0.003
2450765.0964	14.3131	15.186	0.003
2450765.1051	14.5231	15.208	0.003
2450765.1070	14.5686	15.216	0.003
2450765.1089	14.6133	15.222	0.003
2450765.1107	14.6575	15.224	0.003
2450765.1312	15.1483	15.204	0.003
2450765.1330	15.1925	15.199	0.003
2450765.1348	15.2356	15.191	0.003
2450765.1367	15.2803	15.182	0.003
2450765.1385	15.3239	15.175	0.003
2450765.1403	15.3669	15.170	0.003
2450765.1421	15.4106	15.155	0.003
2450765.1440	15.4558	15.143	0.003
2450773.9918	11.8039	14.743	0.005
2450773.9972	11.9328	14.692	0.004
2450773.9999	11.9972	14.652	0.004
2450774.0025	12.0608	14.636	0.004
2450774.0052	12.1236	14.639	0.004
2450774.0078	12.1869	14.627	0.004
2450774.0104	12.2500	14.614	0.004
2450774.0131	12.3133	14.617	0.004
2450774.0201	12.4825	14.595	0.004
2450774.0213	12.5119	14.594	0.004
2450774.0230	12.5511	14.602	0.004
2450774.0241	12.5792	14.621	0.004
2450774.0253	12.6061	14.610	0.004
2450774.0264	12.6342	14.612	0.004
2450774.0276	12.6622	14.614	0.004
2450774.0288	12.6917	14.614	0.004
2450774.0300	12.7189	14.610	0.004
2450774.0311	12.7467	14.611	0.004
2450774.0323	12.7753	14.609	0.004

Table 3—Continued

JD	UT	R	σ_R
2450774.0335	12.8039	14.602	0.004
2450774.0346	12.8314	14.604	0.004
2450774.0358	12.8589	14.602	0.004
2450774.0371	12.8900	14.596	0.003
2450774.0383	12.9194	14.602	0.003
2450774.0395	12.9478	14.593	0.003
2450774.0408	12.9786	14.594	0.003
2450774.0419	13.0064	14.585	0.003
2450774.0431	13.0344	14.583	0.003
2450774.0443	13.0625	14.574	0.003
2450774.0455	13.0908	14.573	0.003
2450774.0467	13.1208	14.572	0.003
2450774.0478	13.1481	14.566	0.003
2450774.0490	13.1753	14.567	0.003
2450774.0501	13.2028	14.566	0.003
2450774.0574	13.3781	14.580	0.003
2450774.0587	13.4081	14.584	0.003
2450774.0598	13.4353	14.590	0.003
2450774.0610	13.4650	14.590	0.003
2450774.0630	13.5128	14.608	0.003
2450774.0642	13.5408	14.616	0.003
2450774.0656	13.5744	14.630	0.003
2450774.0667	13.6019	14.640	0.003
2450774.0679	13.6306	14.646	0.003
2450774.0691	13.6594	14.660	0.003
2450774.0704	13.6889	14.679	0.003
2450774.0715	13.7167	14.682	0.003
2450774.0727	13.7436	14.691	0.003
2450774.0738	13.7714	14.699	0.003
2450775.0445	13.0683	14.642	0.003
2450775.0467	13.1200	14.612	0.004
2450775.0484	13.1617	14.591	0.004
2450775.0500	13.2008	14.584	0.004
2450775.0520	13.2469	14.569	0.004
2450775.0542	13.3019	14.558	0.004
2450775.0560	13.3431	14.574	0.004
2450775.0582	13.3978	14.568	0.004
2450775.0591	13.4175	14.558	0.004
2450775.0598	13.4361	14.560	0.004
2450775.0606	13.4550	14.562	0.004
2450775.0614	13.4742	14.564	0.004
2450775.0622	13.4928	14.567	0.004
2450775.0630	13.5125	14.565	0.004
2450775.0665	13.5956	14.559	0.004
2450775.0673	13.6144	14.557	0.004
2450775.0681	13.6342	14.561	0.004

Table 3—Continued

JD	UT	R	σ_R
2450775.0689	13.6536	14.560	0.004
2450775.0697	13.6728	14.566	0.004
2450775.0705	13.6931	14.562	0.004
2450775.0737	13.7692	14.571	0.004
2450775.0769	13.8461	14.579	0.004
2450775.0801	13.9233	14.583	0.004
2450775.0850	14.0392	14.575	0.004
2450775.0881	14.1133	14.576	0.004
2450775.0914	14.1939	14.559	0.004
2450775.0946	14.2708	14.553	0.004
2450775.0954	14.2903	14.549	0.004
2450775.0989	14.3731	14.539	0.004
2450775.1015	14.4362	14.546	0.005
2450775.1064	14.5539	14.536	0.005
2450775.1088	14.6111	14.551	0.005
2450775.1114	14.6747	14.567	0.005
2450775.1136	14.7275	14.569	0.005
2450775.1159	14.7808	14.605	0.005
2450775.1181	14.8353	14.614	0.005
2450775.1207	14.8978	14.660	0.005
2450775.1232	14.9567	14.689	0.006
2450775.1271	15.0514	14.699	0.006
2450775.1277	15.0642	14.688	0.006
2450775.1283	15.0781	14.689	0.006
2450778.0237	12.5683	14.835	0.015
2450778.0250	12.6003	14.836	0.015
2450778.0264	12.6344	14.832	0.015
2450778.0279	12.6706	14.834	0.014
2450778.0306	12.7350	14.816	0.014
2450778.0315	12.7558	14.805	0.014
2450778.0331	12.7944	14.788	0.013
2450778.0339	12.8144	14.773	0.013
2450778.0348	12.8347	14.769	0.013
2450778.0359	12.8608	14.756	0.013
2450778.0367	12.8800	14.747	0.013
2450778.0379	12.9086	14.737	0.013
2450778.0390	12.9369	14.731	0.013
2450778.0412	12.9900	14.703	0.012
2450778.0423	13.0144	14.680	0.012
2450778.0439	13.0542	14.668	0.012
2450778.0448	13.0764	14.652	0.012
2450778.0460	13.1047	14.641	0.012
2450778.0470	13.1289	14.636	0.012
2450778.0478	13.1478	14.631	0.012
2450778.0487	13.1683	14.620	0.012
2450778.0505	13.2114	14.613	0.011

Table 3—Continued

JD	UT	R	σ_R
2450778.0513	13.2311	14.604	0.011
2450778.0521	13.2503	14.595	0.011
2453328.8286	7.8878	15.773	0.005
2453328.8308	7.9406	15.775	0.005
2453328.8391	8.1367	15.749	0.005
2453328.8457	8.2989	15.722	0.005
2453328.8494	8.3867	15.700	0.005
2453328.8530	8.4733	15.686	0.005
2453328.8567	8.5597	15.671	0.005
2453328.8601	8.6436	15.666	0.005
2453328.8638	8.7308	15.670	0.005
2453328.8672	8.8117	15.679	0.005
2453328.8706	8.8922	15.687	0.005
2453328.8740	8.9758	15.715	0.005
2453328.8806	9.1378	15.761	0.005
2453328.8840	9.2183	15.777	0.005
2453328.8884	9.3219	15.785	0.005
2453328.8918	9.4056	15.756	0.005
2453328.8953	9.4864	15.743	0.005
2453328.8987	9.5672	15.727	0.005
2453328.9021	9.6481	15.717	0.005
2453328.9060	9.7411	15.715	0.005
2453328.9141	9.9383	15.696	0.005
2453328.9175	10.0194	15.702	0.005
2453328.9209	10.1003	15.715	0.005
2453328.9248	10.1931	15.708	0.005
2453328.9280	10.2736	15.704	0.005
2453328.9446	10.6692	15.696	0.005
2453328.9480	10.7500	15.710	0.005
2453328.9570	10.9703	15.715	0.005
2453328.9604	11.0511	15.723	0.005
2453328.9639	11.1325	15.750	0.005
2453328.9673	11.2161	15.749	0.005
2453328.9768	11.4422	15.742	0.005
2453328.9834	11.6028	15.759	0.005
2453328.9854	11.6489	15.752	0.005
2453328.9871	11.6894	15.750	0.005
2453328.9888	11.7297	15.743	0.005
2453328.9905	11.7708	15.734	0.005
2453328.9922	11.8111	15.741	0.005
2453330.7798	6.7144	15.541	0.006
2453330.7833	6.7986	15.555	0.006
2453330.7869	6.8847	15.533	0.006
2453330.7902	6.9653	15.525	0.006
2453330.7970	7.1269	15.504	0.007
2453330.8007	7.2175	15.473	0.006

Table 3—Continued

JD	UT	R	σ_R
2453330.8041	7.2986	15.452	0.007
2453330.8075	7.3792	15.443	0.005
2453330.8108	7.4603	15.439	0.007
2453330.8142	7.5408	15.437	0.006
2453330.8844	9.2251	15.461	0.004
2453330.9140	9.9364	15.503	0.004
2453330.9174	10.0183	15.510	0.004
2453330.9244	10.1864	15.520	0.004
2453330.9278	10.2669	15.515	0.004
2453330.9311	10.3475	15.525	0.004
2453330.9346	10.4283	15.528	0.005
2453330.9380	10.5092	15.528	0.005
2453330.9446	10.6708	15.503	0.004
2453330.9487	10.7678	15.481	0.005
2453330.9548	10.9144	15.442	0.005
2453330.9583	10.9961	15.434	0.004
2453330.9636	11.1264	15.422	0.004
2453330.9670	11.2072	15.424	0.004
2453330.9734	11.3647	15.453	0.004
2453330.9785	11.4861	15.483	0.004
2453330.9834	11.6017	15.513	0.004
2453330.9868	11.6822	15.544	0.004
2453330.9902	11.7675	15.539	0.004
2453330.9919	11.8078	15.537	0.004
2453330.9966	11.9156	15.520	0.004
2453331.0066	12.1617	15.467	0.004
2453331.0100	12.2422	15.461	0.004
2453331.0122	12.2964	15.455	0.004
2453331.0173	12.4172	15.461	0.004
2453331.0190	12.4575	15.457	0.004
2453331.0227	12.5417	15.469	0.004
2453331.0254	12.6061	15.468	0.004
2453331.0327	12.7839	15.463	0.004
2453331.0388	12.9289	15.459	0.004
2453331.0422	13.0144	15.453	0.004
2453331.0466	13.1186	15.461	0.004
2453331.0503	13.2058	15.479	0.004
2453331.0520	13.2461	15.466	0.004
2453331.0540	13.2942	15.470	0.004
2453331.0557	13.3367	15.469	0.004
2453331.0591	13.4172	15.477	0.004
2453331.0625	13.4978	15.481	0.004
2453331.0642	13.5383	15.500	0.004
2453331.0671	13.6114	15.510	0.004
2453331.0688	13.6517	15.506	0.004
2453331.7871	6.8908	15.419	0.005

Table 3—Continued

JD	UT	R	σ_R
2453331.7888	6.9311	15.415	0.005
2453331.7910	6.9842	15.411	0.005
2453331.7927	7.0244	15.411	0.005
2453331.7944	7.0647	15.408	0.005
2453331.8047	7.3100	15.423	0.005
2453331.8064	7.3503	15.421	0.005
2453331.8079	7.3906	15.423	0.005
2453331.8147	7.5517	15.451	0.005
2453331.8164	7.5919	15.450	0.005
2453331.8181	7.6322	15.451	0.005
2453331.8247	7.7936	15.449	0.005
2453331.8264	7.8339	15.452	0.005
2453331.8281	7.8742	15.450	0.005
2453331.8352	8.0414	15.461	0.005
2453331.8367	8.0817	15.452	0.005
2453331.8384	8.1219	15.455	0.004
2453331.8452	8.2831	15.440	0.004
2453331.8467	8.3233	15.430	0.004
2453331.8484	8.3639	15.410	0.004
2453331.8557	8.5383	15.371	0.004
2453331.8574	8.5783	15.360	0.004
2453331.8591	8.6186	15.354	0.004
2453331.8660	8.7825	15.350	0.004
2453331.8677	8.8231	15.345	0.004
2453331.8711	8.9042	15.364	0.004
2453331.8728	8.9444	15.367	0.004
2453331.8745	8.9847	15.376	0.004
2453331.8958	9.4964	15.451	0.004
2453331.8975	9.5367	15.446	0.004
2453331.8989	9.5769	15.437	0.004
2453331.9058	9.7381	15.415	0.004
2453331.9075	9.7783	15.409	0.004
2453331.9092	9.8186	15.400	0.004
2453331.9163	9.9908	15.386	0.004
2456616.6899	4.5589	16.648	0.005
2456616.6958	4.6961	16.657	0.006
2456616.6997	4.7892	16.709	0.007
2456616.7012	4.8339	16.734	0.007
2456616.7031	4.8786	16.751	0.007
2456616.7070	4.9700	16.773	0.008
2456616.7090	5.0214	16.779	0.008
2456616.7148	5.1575	16.799	0.008
2456616.7168	5.2031	16.791	0.009
2456616.7207	5.2956	16.780	0.008
2456616.7271	5.4503	16.687	0.007
2456616.7290	5.4958	16.641	0.006

Table 3—Continued

JD	UT	R	σ_R
2456616.7329	5.5883	16.589	0.005
2456616.7368	5.6811	16.519	0.005
2456616.7427	5.8200	16.492	0.005
2456616.7480	5.9564	16.467	0.007
2456616.7500	6.0019	16.470	0.006
2456616.7520	6.0494	16.480	0.009
2456616.7559	6.1436	16.511	0.010
2456616.7637	6.3247	16.524	0.006
2456616.7720	6.5292	16.605	0.009
2456616.7759	6.6239	16.637	0.009
2456616.7798	6.7194	16.667	0.008
2456616.7866	6.8803	16.732	0.011
2456619.7528	6.0683	15.830	0.004
2456619.7552	6.1258	15.835	0.004
2456619.7596	6.2306	15.837	0.004
2456619.7639	6.3333	15.836	0.004
2456619.7662	6.3878	15.845	0.004
2456619.7707	6.4975	15.864	0.004
2456619.7729	6.5492	15.884	0.004
2456619.7750	6.6003	15.905	0.005
2456619.7773	6.6550	15.906	0.004
2456619.7818	6.7625	15.970	0.004
2456619.7840	6.8153	15.977	0.004
2456619.7863	6.8711	16.012	0.005
2456619.7948	7.0747	16.026	0.005
2456619.7991	7.1781	16.004	0.005
2456619.8012	7.2292	15.977	0.005
2456619.8035	7.2833	15.972	0.005
2456629.6040	2.4969	16.997	0.012
2456629.6060	2.5414	17.019	0.015
2456629.6074	2.5811	17.007	0.013
2456629.6123	2.6986	17.048	0.012
2456629.6143	2.7372	17.079	0.016
2456629.6157	2.7761	17.093	0.012
2456629.6172	2.8150	17.115	0.012
2456629.6191	2.8542	17.115	0.011
2456629.6211	2.9022	17.107	0.013
2456629.6250	2.9964	17.118	0.014
2456629.6270	3.0450	17.115	0.016
2456629.6289	3.0917	17.082	0.017
2456629.6309	3.1408	17.086	0.020
2456629.6367	3.2761	17.018	0.017
2456629.6426	3.4228	16.972	0.022
2456629.6450	3.4828	16.923	0.018
2456629.6699	4.0814	16.853	0.023
2456629.6782	4.2714	16.918	0.019

Table 3—Continued

JD	UT	R	σ_R
2456629.6821	4.3656	17.041	0.016
2456629.6846	4.4328	17.047	0.013
2456637.7035	4.8842	17.219	0.007
2456637.7057	4.9372	17.227	0.007
2456637.7083	4.9986	17.243	0.006
2456637.7111	5.0672	17.281	0.007
2456637.7137	5.1286	17.302	0.008
2456637.7159	5.1814	17.309	0.008
2456637.7181	5.2342	17.323	0.008
2456637.7203	5.2872	17.331	0.009
2456637.7225	5.3400	17.374	0.008
2456637.7249	5.3975	17.381	0.009
2456637.7283	5.4783	17.402	0.010
2456637.7305	5.5319	17.398	0.009
2456637.7327	5.5858	17.398	0.009
2456637.7349	5.6386	17.390	0.009
2456637.7384	5.7225	17.331	0.008
2456637.7406	5.7753	17.307	0.010
2456637.7429	5.8286	17.303	0.008
2456637.7451	5.8819	17.289	0.008
2456637.7473	5.9353	17.253	0.008
2456637.7495	5.9883	17.234	0.008
2456637.7517	6.0411	17.206	0.009
2456637.7539	6.0939	17.202	0.008
2456637.7561	6.1469	17.199	0.008
2456637.7583	6.1997	17.175	0.008
2456637.7605	6.2525	17.157	0.011
2456637.7627	6.3056	17.155	0.009
2456637.7649	6.3583	17.157	0.010
2456637.7702	6.4850	17.151	0.006
2456637.7730	6.5531	17.152	0.008
2456637.7758	6.6203	17.156	0.007
2456637.7786	6.6869	17.171	0.007
2456637.7814	6.7536	17.170	0.008
2456637.7842	6.8203	17.205	0.008
2456637.7870	6.8872	17.224	0.008
2456637.7930	7.0322	17.275	0.010
2456637.7958	7.0994	17.303	0.010

^aThis table will be provided in Machine Readable Format in the online journal version of the paper.